First law of thermodynamics on the boundary for flow through a carbon nanotube

Kazi Ehsanul Karim and BoHung Kim*

School of Mechanical Engineering, University of Ulsan, Daehak-ro 93, Namgu, Ulsan 680-749, Republic of Korea

(Received 18 February 2021; accepted 4 May 2021; published 28 May 2021)

The definition of *boundary* at the nanoscale has been a matter of dispute for years. Addressing this issue, the nonequilibrium molecular dynamics (NEMD) simulations in this work investigate the flow characteristics of a simple liquid in a single-walled carbon nanotube (SWCNT), and equilibrium molecular dynamics simulations support the range of the NEMD results. The inconsistencies in defining the flow boundary at the nanoscale are understood through the first law of thermodynamics: Local thermodynamic properties (the effects of the density distribution, pressure, viscosity, and temperature) define the boundary. We have selected different boundary positions in the CNT to demonstrate the probability of density distribution that also indicates the coexistence of multiple thermodynamic states. Altering the interaction parameters, we produce convergence between the NEMD result and the no-slip Hagen-Poiseuille assumptions. Meanwhile, the results indicate that the boundary position varies between the innermost solid wall and peak density position of the CNT as a function of the input energy or work done in the system. Finally, we reveal that the ratio between the potential energy barrier and the kinetic energy is proportional to the shift of the boundary position away from the innermost solid wall.

DOI: 10.1103/PhysRevE.103.053115

I. INTRODUCTION

Carbon nanotubes, potential quantum wires [1], have startled scientists since their discovery [2]. Variation in the hexagonal honeycomb structures of sp^2 -hybridized carbon nanotubes (CNTs) was the initial inspiration. Gradually, the focus points have converged into quantum transport [3], superfast transportation of molecules [4,5], fuel-cell technology [6], water desalination [7], biosensors [8], and computers [9]. In their experimental studies, Holt *et al.* [10] and Majumder *et al.* [11] unfolded several orders of mass permeability in CNTs of 2–7 nm diameter. Those results were complemented by molecular dynamics (MD) simulations by Hummer *et al.* [12] and Skoulidas *et al.* [13]. Since then, Secchi *et al.* chronicled large and radius-dependent surface slippage in CNTs [14]. The fast transportation phenomenon in CNTs is considerably larger than continuum physics had predicted because of smooth, frictionless surfaces and the curvature effect [5,15]. Consequently CNTs are prominent candidates for computational studies.

The discovery of Kapitza resistance at the nanoscale was an early breakthrough in nanoscience that was confirmed by several studies [16–18]. Interfacial thermal resistance has also been captured in CNTs. Zhong and Lukes [19] indicate that interfacial resistance decreases profoundly as tube-tube contact increases. On the other hand, experimental investigations of CNTs are continually providing new information [20,21]; even the synthesis of CNT forests is being diversified [22,23]. Gradually CNTs have shown to have unique features, including variation in chirality, density, viscosity, friction coefficient, and size effects.

Hagen and Poiseuille derived equations for the rate of pressure-driven flows [24,25]. From a continuum perspective, the equations are based on transforming kinetic energy formalism into a flow to present the flow rate and velocity, ignoring van der Waals (vdW) force and intermolecular potential energy barriers due to their size in the continuum hypothesis. The Hagen-Poiseuille (HP) equations have also been applied in investigations of nanoscale flows in tubes and channels [26–33]. Different approaches have been suggested for establishing pressure-driven flow in computational investigations [32–35]. For instance, Li *et al.* proposed the reflection particle method to induce a pressure-driven flow at the nanoscale [34]. The density, velocity, and pressure in the radial and axial directions in CNTs were previously shown to follow various patterns. Wang and Hadjiconstantinou reported that fluid densities inside CNTs are lower than the bulk density [36]. On the other hand, several studies have shown that fluids within the boundaries of CNTs have layered structures, due to the confinement effect in nanometer-scale regions [28–32]. Still other studies have found that fluid velocity in CNTs is several orders of magnitude higher than the bulk velocity, which eventually produces a higher mass flow rate than in the continuum prediction [28,30–32]. Hanasaki and Nakatani observed that water in CNTs displayed a more pluglike flow than Poiseuille-type flow [37]. Decades ago, Bitsanis *et al.* stated that fluid flow has a negligible effect on the density distribution [38]. Vo *et al.* made the interesting observation that the bin size in a computational study has remarkable effects on the generated results [39]. The bin size and type produce different profiles at the entrances and exits of nanotubes or pores. When a noncylindrical bin is used at the conjunctions of a nanopore and reservoirs, peak density and pressure accumulate at those juxtapositions [40]. The size effect of CNTs is another interesting point in flow

*bohungk@ulsan.ac.kr

 ©2021 American Physical Society

dynamics: Increased velocity, higher slip length, and a larger radial distribution of force occur as tube diameter decreases [28,41]. Sam *et al.* showed that armchair CNTs induce a higher flow velocity than zigzag CNTs [42]. Overall, the evidence shows that the density distribution, type of flow, and the size effect are important in describing nanoscale flow mechanisms.

Viscosity and the friction coefficient predominantly influence the physics of mass transport, just like slip length. At the nanoscale, the intermolecular potential energy (derived as a combination of intermolecular force and the relative positions of molecules) of a nanostructure dominates flow behavior, along with the wall-liquid and liquid-liquid molecular interactions, because the sizes of the wall molecules are comparable to the characteristic physical lengths of the nanoconfined liquid molecules. Hence, slip-modified HP equations are being implemented to accommodate the effects of nanoscale physics on nanotube flow (slip velocity and slip length are considered separately in this regard) [26–33]. To accurately calculate the slip length in a nonequilibrium molecular dynamics (NEMD) simulation, Thomas and McGaughey [31] recommended using a constrained fit with viscosity to measure the slip length and thereby deduce a more precise result, and their recommendation was verified by Kannam *et al.* [33]. On the other hand, Vo *et al.* and Kim *et al.* computed fluid viscosity from shear-driven flow and achieved excellent reliability with other MD simulations and experiments [18,43,44]. Bakli and Chakraborty calculated the slip length for pressure-driven flow and shear-driven flow, along with the comparison [45]. Most important, Thompson and Troian [46] showed a linear region for applying a shear rate to prevent exponential growth of the slip length. From an equilibrium molecular dynamics (EMD) viewpoint [47], Bocquet and Barrat [48] were the first to calculate the viscosity and slip length, by applying the Green-Kubo linear response theory. Afterward, some studies showed the inconsistency of that method when considering systems of finite size. Periodic boundary conditions for CNTs [32] or generalized Langevin equations are being applied to overcome that problem [49–52]. On the other hand, negative slip length has also been reported in several studies [53–55]. Well-bound and adsorbed fluid layers over solid walls are responsible for resembling the negative velocity slip length. Despite all of that work in analyzing the nanoscale flow, defining the boundary position remains a critical focus.

An analysis of the flow characteristics depends on the definition of the wall-liquid boundary and the accurate application of boundary conditions. Different boundary positions have been proposed to explain and predict nanoscale phenomena. Following the understanding of continuum physics, the position of the solid-liquid boundary in a nanochannel was defined as the innermost solid layers [39,56–58]. Another popular standpoint is to define the boundary in the nanoscale as the first peak density or absorption layer position in the layered structure of liquids adjacent to the solid surface [59–63]. The Gibbs dividing plane, interfacial thermal resistance, thermal conductivity, slip velocity, and other intrinsic properties have been used as the basis for boundary definitions. However, the intriguing question remains, what are the reasons behind such discrepancies and where is the boundary at the nanoscale?

To address that question, we observed flow characteristics from the continuum perspective to the nanoscale and analyzed our observations from the stance of the law of conservation of energy to define the boundary at the nanoscale. We used NEMD simulations to analyze a pressure-driven flow of a simple liquid through a single-walled carbon nanotube (SWCNT). We also conducted EMD simulations to check the range of the thermodynamic properties acquired from the NEMD simulations. To examine the limitations of the continuum Hagen-Poiseuille (HP) assumptions and the validity of modified HP assumptions for the nanoscale, we acquire the local viscosities of a simple liquid from the shear-driven flow simulations. The density of a simple liquid in a carbon nanotube (CNT) was measured with different sizes of cylindrical bins, to consider the layered structures and the coexistence of solid, liquid, and gaseous states. A no-slip based continuum HP assumption has been achieved at the nanoscale, by applying the concept of the conservation of energy. In the end, we were able to approximate the position of the boundary in a nanosized system containing various viscosities, pressure drops, and temperatures. The first law of thermodynamics provides sustainable reasoning to explain the inconsistencies found when defining the boundary position at the nanoscale.

II. THEORETICAL BACKGROUND

Hagen and Poiseuille separately derived equations for pipe flow and blood flow, and Hagenbach then provided the popular format for HP flows from the Navier-Stokes (NS) equations [24,25,64,65]. Poiseuille acknowledged what are now called entrance effects without considering the relative roles of inertial and viscous forces. However, Stokes [65] theoretically justified the HP law and concluded that it was one of the exact solutions of the NS equations [24]. The boundary conditions assume (i) an incompressible fluid (density is constant and uniform, $\nabla \cdot \tilde{\mathrm{V}} = 0$) is in a steady ($\nabla \cdot \rho \vec{V} = 0$), Newtonian, laminar, and unidimensional flow; (ii) the length of the pipe is substantially larger than the diameter; (iii) the fluid does not accelerate in the pipe; and (iv) the flow is fully developed. The initial form of a Poiseuille flow is shown in Eq. (1),

$$Q = \frac{K'' D^4 P}{L}, \tag{1}$$

where K'' is a constant, a function of temperature and the type of liquid; Q is the volumetric flow rate; P is the pressure producing the flow; and L is the pipe length. The HP equations formalize the total kinetic energy of a continuum pipe system into a flow rate Q and velocity $V_{z,r}$ as shown below,

$$Q_{(\mathrm{HP})} = \frac{\pi R^4}{8\mu}\frac{\partial P}{\partial Z}, \tag{2}$$

$$V_{z,r\,(\mathrm{HP})} = \frac{R^2}{4\mu}\left(1 - \frac{r^2}{R^2}\right)\frac{\partial P}{\partial Z}, \tag{3}$$

where R is the pipe or tube radius, μ is viscosity, and $\partial P/\partial Z$ is the pressure gradient.

Slip length is added to predict the nanoscale flow rate because no-slip boundary conditions do not exist at the nanometer scale. The slip length accounts for the effects of

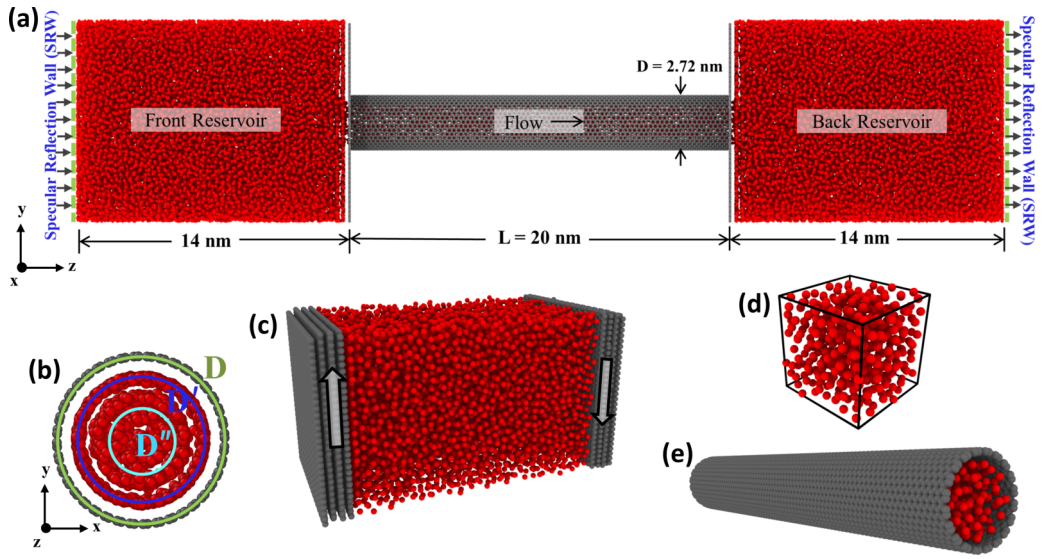

FIG. 1. (a) Schematic diagram of the flow of liquid argon through a carbon nanotube (CNT); (b) inset of the CNT with the three probable boundary positions; (c) liquid argon sheared between graphene walls; (d) liquid argon molecules in a periodic cubic box; (e) CNT filled with liquid argon for analysis in an equilibrium molecular dynamics simulation.

the solid-liquid interface and molecule size. From the perspective of the input energy and thermodynamic states at the nanoscale, transforming kinetic energy formalism into a flow rate must consider the slip at the solid-liquid interface because the interactions between the wall and liquid molecules differ noticeably from those in classical liquid transport equations. Moreover, the intermolecular forces of the wall molecules, the thermal or velocity slip, and the discreteness of the liquid molecules near the solid surface play vital roles in nanoscale physics [66]. In short, it can be anticipated that the flow inside CNTs will exhibit a slip tendency; thus the volumetric flow rate was modified [31] as shown in Eq. (4),

$$Q_{(\mathrm{MHP})} = \frac{\pi (R^4 + 4R^3 L_s)}{8\mu} \frac{\partial P}{\partial Z}, \tag{4}$$

where L_s is the slip length. Still, predicting the velocity profile at the nanoscale using bulk-scale equations requires modification from two perspectives: slip velocity and slip length. Modification in terms of the slip length (L_s) is achieved by applying the Stokes equation and Navier boundary conditions [31,33], as given in Eq. (5), whereas the slip velocity (V_s) modification upgrades the no-slip HP assumption to produce a velocity profile adjacent to nanoscale predictions with slip, as given in Eq. (6) [33,40]:

$$V_{z,r(\mathrm{MHP})} = \frac{R^2}{4\mu}\left(1 - \frac{r^2}{R^2} + \frac{2L_s}{R}\right)\frac{\partial P}{\partial Z}, \tag{5}$$

$$V_{z,r(\mathrm{MHP})} = \frac{R^2}{4\mu}\left(1 - \frac{r^2}{R^2}\right)\frac{\partial P}{\partial Z} + V_S. \tag{6}$$

The Navier boundary condition, which has been widely adopted as the boundary condition at the nanoscale and justifies the slip behavior at the wall-liquid interface, is shown in Eq. (7).

$$V_s = L_s \frac{\partial v}{\partial z}\bigg|_{\mathrm{wall}}, \tag{7}$$

where $\partial v/\partial z$ is the velocity gradient. Therefore, it is necessary to implement both modified Hagen-Poiseuille (MHP) equations.

III. MOLECULAR DYNAMICS SIMULATION

The arrangements required to analyze a simple liquid [67] flow in an MD simulation are depicted in Fig. 1, where liquid argon is used as the simple liquid flowing along a CNT. Initially, 64 800 molecules of the simple liquid were placed for transport from the front reservoir (FR) to the back reservoir (BR) through the nanotube. An armchair (20, 20) CNT, 20 nm in length (L) and 2.72 nm in diameter (D), was placed at the center ($x = 0$, $y = 0$, $z = 14 - 34$ nm) of the simulation box parallel to the xy plane. Two 10 nm $\times$ 10 nm graphene membranes (GMs) were placed at the open ends of the CNT, to construct the fluid reservoirs. Periodic boundary conditions were applied in the directions of the x and y axes in the simulation domain. With a view to preventing disruption of the thermodynamic properties of the molecular level system by a natural wall piston (due to van der Waals interactions between the piston and simple liquid), pressure-driven flow is induced using specular reflection walls (SRWs) [34,40,68,69]. An SRW is a physically simple, computationally effective method and bulk flow regions become independent after colliding with the reflective membrane [40,68,69]. Two SRWs were placed at the ends of the front and back reservoirs along the xy plane. At the beginning of each simulation, the SRWs and GMs were placed around 15 nm away in the direction of the z axis, and the number density of the simple liquid was confirmed to be $\rho_{\mathrm{bulk}} = 0.8$. However, the generated results are shown for reservoirs that are 14 nm away from the GMs for continuity in presenting the results from all the simulations because the SRW of the FR is moving toward the GM and the SRW of the BR is moving away from it. Three boundaries are presented in Fig. 2(b): The tube diameter (D), peak density diameter (D'), and 3σ reduction diameter (D'') provide

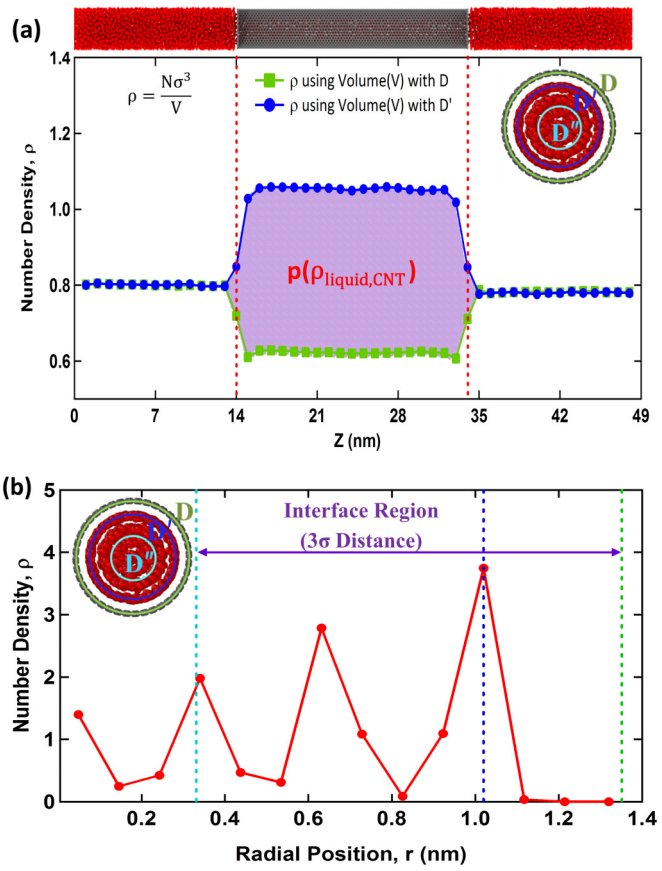

FIG. 2. (a) The density distribution of argon along the axial flow direction; (b) the density distribution of argon in the radial position.

simple and reasonable explanations for the HP equations at the nanoscale, enabling the boundary condition to be applied at various places for validation and analysis of the MHP.

The interatomic interactions between argon molecules were measured using the truncated Lennard-Jones (12−6) potentials given by

$$V_{\text{truncated}}(r_{ij}) = 4\varepsilon\left[\left\{\left(\frac{\sigma}{r_{ij}}\right)^{12} - \left(\frac{\sigma}{r_{ij}}\right)^{6}\right\} - \left\{\left(\frac{\sigma}{r_c}\right)^{12} - \left(\frac{\sigma}{r_c}\right)^{6}\right\}\right], \tag{8}$$

where ε is the depth of the potential well, r_{ij} is the intermolecular distance between molecules i and j, σ is the diameter of molecules (the finite molecular distance at which the interatomic potential is zero), and r_c is the cutoff radius for atomistic interactions. The intermolecular forces are truncated at a distance of $r_c = 1.0$ nm, approximately 3σ. The adaptive intermolecular reactive empirical bond order (AIREBO) potential is used for the interatomic interactions between the carbon atoms in the CNT and GMs. The interaction parameters between carbon and argon molecules are assessed using the Lorentz-Berthelot (LB) mixing rules [70]. The interaction parameters used in this study are presented in Table I. The simulations were conducted with the Maxwell-Boltzmann velocity distribution at 100 K temperature to engage the random thermal velocities of liquid molecules. Equilibrium of the

TABLE I. Intermolecular interaction parameters used in this study.

Interaction	ε (eV)	σ (nm)
Ar-Ar	0.0103	0.3405
C-Ar	0.005	0.3403

system was achieved by the NVT ensemble and Nosé-Hoover thermostat. At equilibrium, the velocity distribution at the point of measure should follow the normal distribution with convergence to the zero skewness and kurtosis [17,71–74]. For this purpose, higher moments of the velocity distribution were calculated and normal distribution was confirmed with the skewness and kurtosis. The number of molecules per bin in the CNT varied significantly due to the existence of multiple phases [29]. Thus local thermal equilibrium (LTE) was confirmed by skewness and kurtosis along with the ergodic hypothesis, ensuring the ensemble average over time. Convergence of the moments of kinetic energy of the molecules up to fourth order also confirmed the ergodicity of our system [75,76]. The Nosé-Hoover thermostat was applied to ensure a constant system temperature at 100 K with two subsequent canonical (NVT) ensembles. The initial state with the NVT ensemble was equilibrated for 25 ns with a 1 femtosecond (fs) time step to establish the equilibrium MD simulations. In the second NVT ensemble, a flow was induced across the simulation domain by moving the SRWs at constant velocity (U_M) along the z axis, while the carbon atoms of the CNT and GMs vibrated about a fixed lattice point. In addition, the GMs were kept static (at $z = 14$ and 34 nm) throughout the entire simulation by fixing the twenty carbon atoms at the edges of the GMs at their initial positions. The simulation was conducted for a duration of 1–5 ns, depending on the velocity of the SRWs. The Verlet algorithm was used to integrate the equations of motion [70]. All of the simulations were performed in LAMMPS [77]. The Irving-Kirkwood (IK) expression [78,79] was used for the pressure calculation, to consider three orthogonal stresses in the x, y, and z directions across the simulation domain (S_{xx} , S_{yy}, and S_{zz}). The pressure tensor for an N particle system is calculated by the following formula to consider kinetic and virial contributions:

$$S_{\alpha\beta} = \frac{1}{V}\left\langle m^i\left(v_\alpha^i - u_\alpha\right)\left(v_\beta^i - u_\beta\right) + \frac{1}{2}\sum_{i,j}^{N}\left(r_\alpha^i - r_\beta^i\right)f_\beta^{i,j}\right\rangle, \tag{9}$$

where the first and second terms on the right side are the kinetic and virial components, respectively. In the kinetic part, m is the mass of atom i, v is the velocity of atom i, and u is the streaming velocity in the α and β directions of the Cartesian coordinate system. In the virial part, $(r_\alpha^i - r_\beta^i)$ is the relative distance vector between the atoms i by atom j, and $f_\beta^{i,j}$ is the intermolecular force acting on atom i from atom j.

Bulk and local interfacial viscosities were measured using an MD simulation of shear-driven flow [18,43,44], as shown in Fig. 1(c). Liquid argon molecules were replicated in a three-dimensional channel with a height of 11.3 nm and a width of 6.6 nm, and the velocity of the GMs was set to 50 m/s. At this point, the system configuration was kept in a state similar to

that in the CNT flow simulation. The shear rate of the solid wall was kept within the linear regime. The local dynamic viscosity of the liquid was measured as the ratio of the shear component of the stress tensor (S_{xz}) and the applied shear rate ($\dot{\gamma}$):

$$\mu = -\frac{S_{xz}}{\dot{\gamma}}, \tag{10}$$

where the stress tensor is measured in the simple liquid domain. The per-atom array values were acquired as the products of the stress and volume units. Thus, the local stress in each slab bin (S_{xz}^{bin}), positioned parallel to the GMs, was calculated as the ratio of the average total per-atom stress tensor by the particular volume of the slab bin (V_{bin}), $S_{xz}^{\text{bin}} = (S_{xz}N_{\text{bin}})/V_{\text{bin}}$, where N_{bin} is the number of atoms in each slab bin. Data were collected and averaged after ensuring an isothermal steady state, using 1 fs as the time step. The measured local viscosity can be applied in general flow problems because the shear rate is in the linear regime.

EMD simulations were conducted for a box of liquid argon and the armchair (20, 20) CNT filled with liquid argon. The simulation domains are shown in Figs. 1(d) and 1(e). One periodic cubic box of simple liquid with 0.8 number density is simulated for 10 ns along with 10 ns of data averaging. The Green-Kubo formula, given as Eq. (11) below, was used to calculate the autocorrelation of the pressure tensor to viscosity [80]. For the EMD simulation in the CNT, the liquid reservoirs were removed and a periodic boundary was implemented along the flow direction of the CNT. Shear viscosity was measured by Eq. (11), autocorrelating the off-diagonal elements of the pressure tensor. The friction coefficient, λ, was determined by the Green-Kubo relation for the force autocorrelation function, as shown in Eq. (12) [48,49]. A larger correlation length was used for the Green-Kubo calculation and data were acquired for 8 ns from the converged plateau after 2 ns. In brief, the friction coefficient λ and viscosity μ were obtained from the running integral of the force and pressure autocorrelation functions, respectively:

$$\mu = \frac{V}{K_B T}\int_0^\infty \langle P_{\alpha\beta}(t_0)P_{\alpha\beta}(t_0+t)\rangle_{t_0} dt, \tag{11}$$

$$\lambda = \frac{1}{AK_B T}\int_0^\infty dt\,\langle F_w(t)F_w(0)\rangle_{\text{equ}}, \tag{12}$$

where K_B is the Boltzmann constant, V is the volume, T is the temperature, $P_{\alpha\beta}$ is the off-diagonal element of the pressure tensors (α, β is the x, y, and z directions), A is the lateral area in the CNT, and F_w is the total lateral force acting on the CNT surface by the liquid argon. In the CNT, P_{xz} is considered for the viscosity calculation.

IV. RESULTS AND DISCUSSION

A. Density and pressure distribution of the simple liquid

Intermolecular forces and the structures of nanoscale systems affect the thermodynamic properties of a confined simple liquid. The density distributions of liquid argon display different patterns, as shown in Fig. 2. A cylindrical bin was applied in the simulation domain along with the CNT periphery, which was divided into several slab bins. The thickness of each bin, Δz, was 1 nm in the axial (z) direction of the flow to calculate the number density, $\rho = N\sigma^3/V$ of the simple liquid. The obtained data are averaged for 1 ns during the equilibrium condition. The tube diameter (D) was used for the cylindrical bin configuration throughout all the calculations and analysis of this paper. However, a variation in the configuration of the cylindrical bin was adapted only for the analysis of the number density of liquid argon in the axial (z) direction. The number density with the tube diameter (D), ρ_D, of the simple liquid in the CNT along the axial (z) direction has a lower value than in the bulk region, ρ_{bulk}; thus, $\rho_D < \rho_{\text{bulk}}$. On the other hand, a higher number density for the liquid in the CNT was achieved when considering the peak density diameter (D') for the bin configuration, $\rho_{D'} > \rho_{\text{bulk}}$. In Fig. 2(a), the probability of the density distribution for the simple liquid confined in the CNT, $p(\rho_{\text{liquid,CNT}})$ is shown in the highlighted region. The multiple phases of the liquid in the CNT [29] can also be interpreted using $p(\rho_{\text{liquid,CNT}})$. Here, the $\int_{z_1}^{z_2} |\rho_{D'} - \rho_{\text{bulk}}|dz$ region indicates the coexistence of solid and liquid states, whereas the $\int_{z_1}^{z_2} |\rho_{\text{bulk}} - \rho_D|dz$ region represents the coexistence of liquid and gas states, where $z_1 = 14$ nm and $z_2 = 34$ nm in the computational domain. One possible form of the probability function for the number density, $p(\rho_{\text{liquid,CNT}})$, is

$$p(\rho_{\text{liquid,CNT}}) = \{\rho_{\text{liquid,CNT}}(z):\ \rho_D \leqslant \rho_{\text{liquid,CNT}} \leqslant \rho_{D'}\}. \tag{13}$$

Although varying the selection of the maximum radius for the cylindrical bin $r_{\max}$ changed the results by including or excluding the interfacial empty region or depletion length, it can also be considered to represent the multiple phases of the liquid in the CNT. Consequently, considering only the tube diameter (D) in the axial density calculation could underestimate the overall density distribution, $\rho_{\text{liquid,CNT}}(z)$. For this reason, It is more appropriate to describe the axial (z) density distribution as a probability function $p(\rho_{\text{liquid,CNT}})$ to illustrate the coexistence of solid, liquid, and gaseous states in the CNT. The layered structure of liquid argon is exhibited in Fig. 2(b) along the radial (r) direction as an example of the nanoconfinement effect. The coexistence of multiple phases in the CNT can be approximated from this figure as well. Strong wall-liquid interactions in the vicinity of CNT explain the higher number density at the interfacial region, $\rho_{\text{interface},r}$. Three boundaries, tube diameter (D), peak density diameter (D'), and 3σ reduction diameter (D''), are also indicated in Fig. 2(b). Because the diameter of CNT confinement is 2.72 nm, subtracting the 3σ distance produces a bulk region of approximately 0.7 nm in the CNT. The radial density profile, $\rho_{\text{CNT}}(r)$, also indicates that the viscosity near the periphery of the CNT, $\mu_{\text{interface}}$, would be larger because it poses a larger density layer. In the interfacial region of the CNT, $\rho_{\text{interface,r}}$ is approximately five times larger than ρ_{bulk}. In consequence, the system is validated with the expected bulk density of liquid argon, $\rho_{\text{bulk}} = 0.8$, and a better representation of the axial liquid density in CNT is proposed with the probability function of the density distribution, $p(\rho_{\text{liquid,CNT}})$.

Different pressure drops (ΔPs) were induced by moving the SRWs, as shown in Fig. 3. The average of the three orthogonal normal stress components from the IK expression was

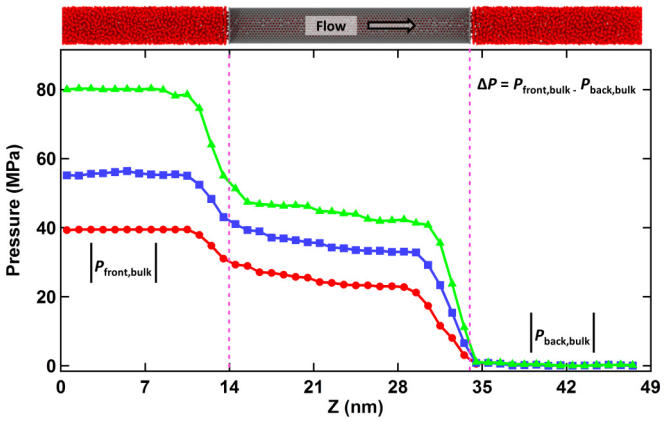

FIG. 3. The pressure distribution of argon along the axial flow direction.

used to calculate pressure of the system. The data for every 0.5 ns were averaged to calculate the pressure drop, $\Delta P = \Delta P_{\text{front,bulk}} - \Delta P_{\text{back,bulk}}$, between the two reservoirs. The flow characteristics were analyzed with induced pressure drops of 39.3, 55.2, and 80.5 MPa when the system temperature was maintained at $T = 100$ K. Multiple velocities (1, 2, and 3 m/s) were set for the SRW to induce different ΔPs. Pressure drops along the axial direction (z) varied significantly at the entrance and exit of the CNT. On the other hand, a gradual decrease in the pressure gradient can be observed inside the CNT in Fig. 3. Larger pressure drops occur at the entrance and exit of CNT as the induced ΔPs increase. When a larger ΔP is induced, the pressure in the CNT also rises, but it slopes gradually. The pressure drop develops by means of adjustments in the relative positions of simple liquid molecules in the corresponding reservoirs.

B. Deduction of the continuum assumption for nanoscale phenomena

Slip is the most pertinent characteristic of nanoscale physics. Thus, a no-slip deduction in nanoconfinement requires an alteration of its fundamental thermodynamic property. The slip velocity, V_s, in nanofluidics indicates the presence of strong kinetic energy (E_K) in the liquid molecules at the wall-liquid interface. Thus, an increase in the wall-liquid interatomic potential energy will reduce the kinetic energy at the wall-liquid interface, as established by the first law of thermodynamics, or the law of conservation of energy, as shown in Eq. (14):

$$Q + W = \Delta E_P + \Delta E_K, \tag{14}$$

where W is the work done on the system, $\int PdV$; Q is the heat added to the system, $m \int cdT$; E_P is the intermolecular potential energy, $\sum V(\vec{r}_{i,j})$; E_K is the kinetic energy, $\sum \frac{m_i \vec{v}_i^2}{2}$; and Δ represents a change of energy. The interaction parameter, thus wettability, plays a critical role in nanoscale phenomena. The van der Waals interaction contributes as a primary force field to govern the interfacial thermodynamic properties. In this regard, the LB mixing rule [70] provides the closest approximation; however, comparison with experimental results and variations in the phenomenological assumptions are desirable. Therefore, adjustment of wettability unlocks different physical aspects to visualize, for instance, deduction of the continuum assumption for our nanoscale flow. In this regard, a trial of different increments of wettability was applied to reach the desired no-slip case. Adapting the wettability using a ten-times increment from the LB mixing rule [70] as the wettability value ($\varepsilon_{No-\text{Slip}} = 10\varepsilon_{\text{C-Ar}}$) deduced the no-slip condition of the fundamental HP equation. As mentioned before, the molecular interaction strength within the CNT confinement played the vital role for convergence to the no-slip condition of HP equation. The existence of attractive and repulsive forces, along with the interaction energy of molecules, strongly distresses nanoscale flow behavior, which is why the continuum no-slip assumption of the HP equation breaks down. In the no-slip deduction through increased wettability, the acquired radial velocity is found within the no-slip HP assumption of D and D', as shown in Fig. 4(a). This

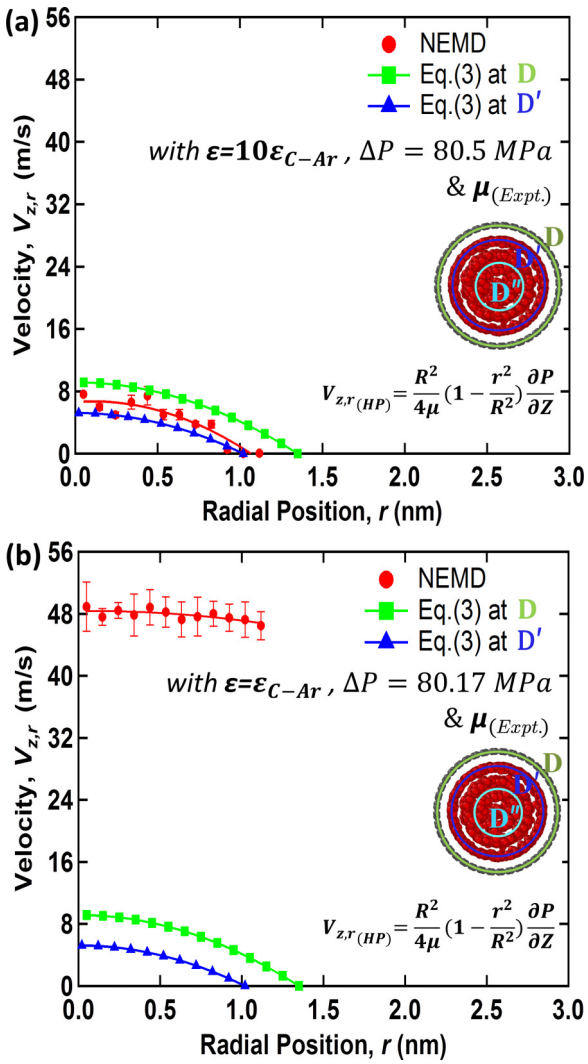

FIG. 4. A comparison of the velocity profile from the NEMD simulations and the continuum Hagen-Poiseuille (HP) assumption at different boundary positions: (a) No-slip interpretation by modifying the interaction strength from the Lorentz-Berthelot (LB) mixing rule, and (b) without altering the interaction strength from the LB mixing rule.

shows how wettability tuning can deduce the original HP flow, even at the nanoscale. Dynamic structuring and oscillatory density of liquid occur at 3σ proximity of the solid-liquid interface: stacking of liquid molecules near the solid wall and van der Waals (vdW) forces between wall and liquid atoms are the explanations behind such phenomena [81,82]. For strong intermolecular interaction strength, adsorbed and immobile fluid layers were reported at the solid-liquid interface. In those scenarios, negative slip length was evident [53–55]. Thus, dynamic structuring acts as the principal characteristic at the solid-liquid interface and controls the slip condition. Higher pressure difference, as input energy, transforms the negative slip condition into a no-slip condition. Therefore, a large pressure drop, $\Delta P = 80$ MPA, was required to make the liquid flow in the CNT during the wettability manipulation. When the interaction strength increased in the nanoconfinement, it imposed a very strong energy barrier with increased potential energy, so, to enable the kinetic flow, more work done $\int pdV$ was required. Thus higher pressure, along with the wettability adjustment, was the key to establishing that observation. In short, the magnitude of wettability and energy at the solid-liquid interface decides whether the system will possess negative-slip or no-slip or positive-slip condition. Figure 4(b) shows the computational results with the LB interaction strength. Comparing Figs. 4(a) and 4(b) shows a difference in interaction strength of ten times, resulting in around a sevenfold variation in the velocity at the center of the CNT. Remarkably, the deduced no-slip NEMD result indicates that the boundary position (BP) is between D and D', $D < \mathrm{BP} < D'$

C. Effects of local viscosity and slip on flow characteristics in the comparison between continuum and nanoscale phenomena

Variations in local viscosity and slip affect flow behavior enough to break down the continuum hypothesis at the nanoscale. Therefore, those thermodynamic properties permit a close analysis of the flow behavior that segregates continuum and nanoscale physics. Figure 5(a) shows the radial velocity profile with the variations in viscosity for the no-slip HP equation, and Fig. 5(b) presents the slip velocity MHP equation. Bulk viscosity was measured as $1.82 \pm 0.185 \times 10^{-4}$ Pa s from the shear-driven flow and Green-Kubo linear response theory, as shown in Figs. 1(c) and 1(d), respectively. The viscosity at the interface of the shear-driven flow in Fig. 1(c) is $3.31 \pm 0.216 \times 10^{-4}$ Pa s, which is a close match with the result of a previous computational study [40]. The high value of the interface viscosity,$\mu_{\mathrm{interface}}$, points toward the dynamic structuring of liquid argon. Interactions between carbon and argon molecules, $\varepsilon_{\mathrm{C-Ar}}$, induce a high local viscosity in the interfacial region. The viscosity measured in the EMD simulation in CNT, $\mu_{\mathrm{Ar,CNT}}$, in Fig. 1(e), is $2.33 \pm 0.17 \times 10^{-4}$ Pa s. Because the whole region of the simple liquid in the CNT is considered during the EMD computation, the bulk and interfacial regions both affected the result. On the other hand, the experimental viscosity for liquid argon is 2×10^{-4}Pa s [60]. Experimental, bulk, and interface viscosities have all been considered in analyzing the effect of viscosity. The NEMD result and the no-slip HP assumption differ by several orders, as shown in Fig. 5(a), due to the presence of intermolecular forces during nanosized confinement. The effects of van der Waals (vdW) forces at the molecular level explain the divergence from the continuum-scale prediction. The NEMD results are presented to show the pressure drop, $\Delta P = 55.2$ MPa. Close observation of Fig. 5(b) reveals that the MHP with $\mu_{\mathrm{interface}}$ produces a reasonably close approximation of the NEMD result.

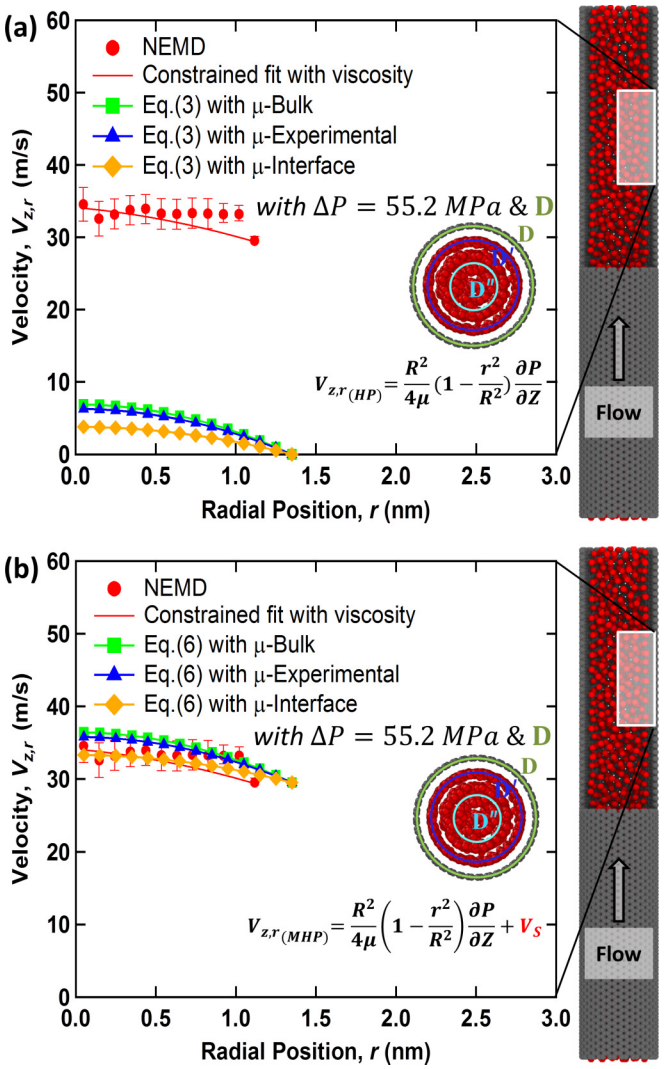

FIG. 5. Effect of local viscosity on the comparison of velocity profiles at different flow regions: (a) Velocity profile from the NEMD simulation and fundamental Hagen-Poiseuille (HP) assumption; (b) velocity profile from the NEMD simulation and slip velocity added modified Hagen-Poiseuille (MHP) assumption.

Figures 6(a) and 6(b) show the slip length (L_S) calculations for two ΔPs along with the boundaries D and D'. No-slip HP assumptions are also presented to show the shortfall of the fundamental HP assumption at the nanoscale. The velocity profile of liquid argon was acquired using a cylindrical bin whose radius corresponds to the radius of the CNT (1.36 nm), with a view to achieving the axisymmetric geometry of the CNT and superior statistical accuracy. Fully developed regions in the CNT were considered during the data collection. The cylindrical bin was divided into six, eight, and ten concentric circle bins from the z axis to acquire

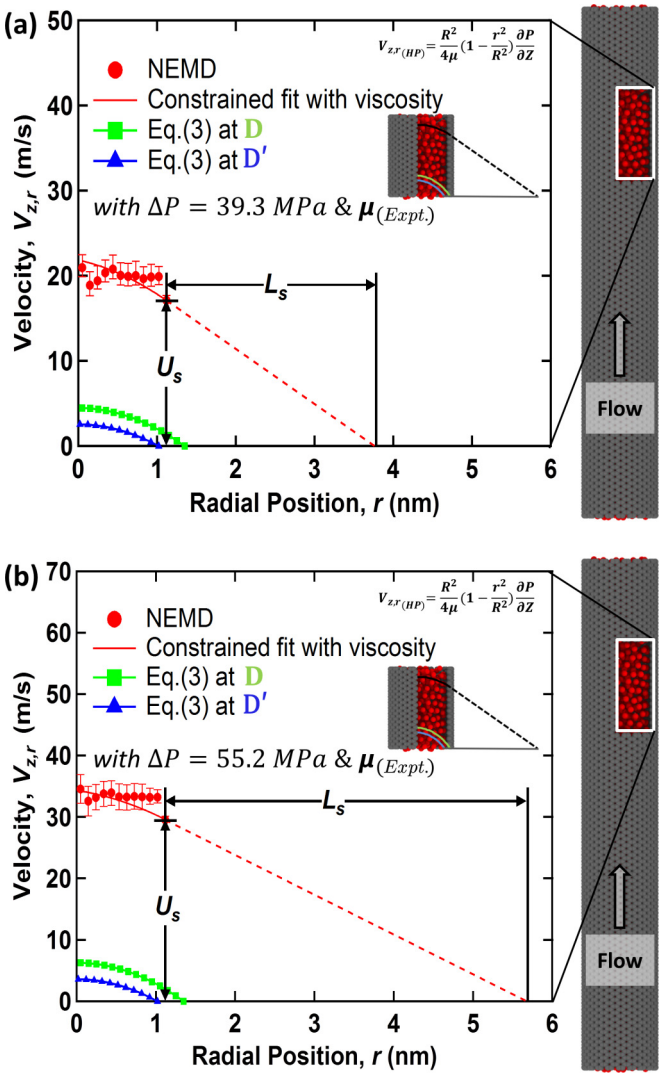

FIG. 6. Breakdown of the continuum Hagen-Poiseuille (HP) assumption at the nanoscale, along with the slip length calculation for (a) $\Delta P = 39.3$ MPa, and (b) $\Delta P = 55.2$ MPa.

the velocity data in the radial direction of the CNT. Then the NEMD data from those three concentric circle bins during different instantaneous simulation times were averaged to produce the liquid argon velocity profile inside the CNT. The slip length is calculated from the velocity profile with a constrained quadratic regression (second-order polynomial curve fitting [v(r) $= ar^2 + br +$ c] and the Navier boundary condition, Eq. (7). The slip length is calculated on the basis of Ref. [31], within the critical shear rate. The value of experimental viscosity was used for the constrained curve fitting. A difference in slip length prediction is observed between the constrained and unconstrained curve fitting, as previous studies reported [31,33]. However, due to the comparatively smaller slip length with our molecular system, the overall discrepancy between the constrained and unconstrained results was small. The slip length achieved from the NEMD is 3.5 $\pm$ 1 nm. The predicted radial velocity is very small when considering the D'' boundary (3σ reduced diameter); thus $V_{D''}$ is not presented in this work. The slip length ($L_{S,\mathrm{NEMD}}$) measured in the CNT is smaller than in other works in the literature that considered liquid argon [28]. The system temperature and aspect ratio (diameter to length ratio) explain that discrepancy. Higher aspect ratios and temperatures produce a higher flow rate, and thus a higher slip length [30,41]. The CNT system in this paper ran at 100 K and had a 7.4:1 aspect ratio, whereas the previous reports used a system that ran at 120 K and had a 20.5:1 aspect ratio [28]. To check the range of our result, the friction coefficient (λ) was also measured from the EMD simulation using Green-Kubo theory to establish the force autocorrelation function, as shown in Fig. 1(e) and Eq. (12). The value of the friction coefficient (λ) from the converged plateau of the running integral in the EMD is $7.71 \pm 1 \times 10^4\,\mathrm{kg\,m^{-2}\,s^{-1}}$. That value corresponds to a slip length of 3.45 ± 0.4 nm. The simple liquid reservoirs were removed and periodic boundary conditions were applied to simulate an infinitely long CNT, and thereby avoid the finite size issue in the EMD. Therefore, the slip is evidence that the nanoconfinement effect causes the continuum hypothesis to break down and variations in local viscosity play an important role in justifying modification to the continuum prediction.

D. Defining the boundary at the nanoscale from the viewpoint of the conservation of energy

The inconsistencies among the no-slip HP assumption, the MHP prediction, and the computational result are important in analyzing the BP of liquid flow through a CNT. The position of the boundary in the no-slip NEMD deduction has been discussed previously in comparison with the continuum HP assumption, $D <$ BP $< D'$. The comparison between the MHP and NEMD results is the remaining window from which to view the BP without any alteration.

First, consider two existing modifications of HP equations, the MHP. Figures 7(a) and 7(b) present the MHP by slip length cases with $\Delta P = 39.3$ MPa and $\Delta P = 55.2$ MPa, respectively, and Figs. 7(c) and 7(d) add the slip velocity to the MHP with the corresponding ΔPs. Both MHPs are presented with the prediction by nanotube diameter (D) and peak density diameter (D') to analyze the disparity. The flow prediction of both MHPs varies between D and D'. However, the calculated slip length (L_S) from the slip velocity added MHP is very inconsistent. For example, the NEMD slip length with $\Delta P = 55.2$ MPa is 4.56 nm whereas the slip velocity added MHP predicts the slip length to be 3.17 and 4.19 nm for the boundaries of D and D', respectively: $L_{S,\mathrm{NEMD}} \neq L_{S,D} \neq L_{S,D'}$. More precisely, the slip velocity added MHP is an attempt to make the NEMD velocity profile close to the theoretical prediction but it cannot predict the slip behavior accurately. Slip length (L_S), an intrinsic thermodynamic property, is directly related to the flow behavior of different materials. Because the slip velocity added MHP does not consider the friction coefficient and thereby omits slip length from its prediction, it is not appropriate for the boundary assumption. Nonetheless, it indicates that the boundary is near the peak density position (D'). The slip length added MHP is derived from the Stokes equation and predicts the slip length accurately while applying the Navier boundary condition in Eq. (7). In this case, the slip length perfectly matches the NEMD result for both boundary positions, D and D': $L_{S,\mathrm{NEMD}} = L_{S,D} = L_{S,D'}$. However,

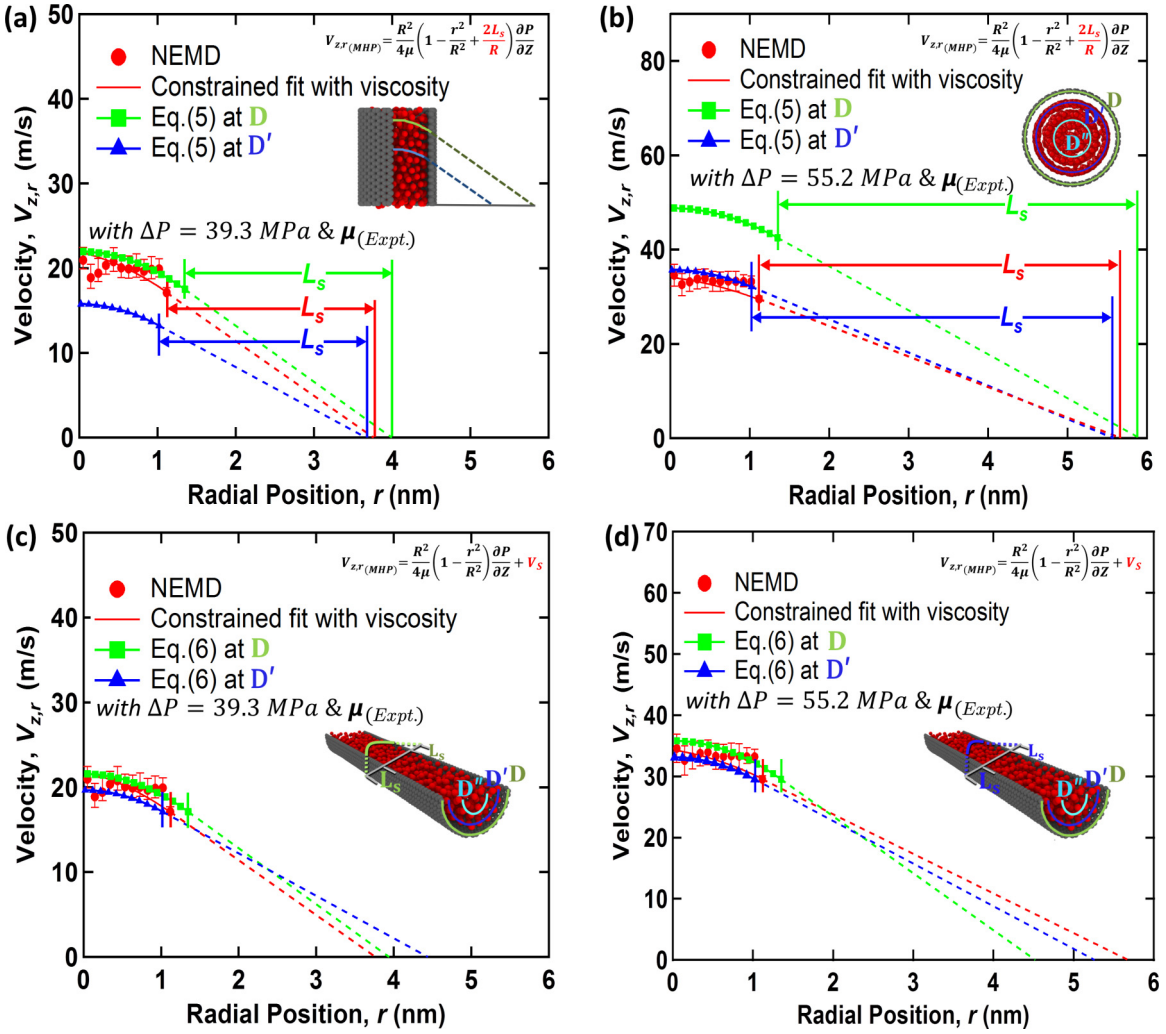

FIG. 7. A comparison of the velocity profile from the NEMD simulations and the modified Hagen-Poiseuille (MHP) equations when varying the pressure drop ΔP: (a), (b) MHP by slip length with $\Delta P = 39.3$ and 55.2 MPa, respectively; (c), (d) MHP by slip velocity with $\Delta P = 39.3$ and 55.2 MPa, respectively.

an interesting consequence has been observed in this regard. Applying a low pressure drop produces a flow boundary close to the D position, or around the innermost solid wall. On the other hand, the flow boundary shifts to D' when higher ΔP is applied within the linear shear region. Therefore, it can be understood that the slip length added MHP is reliable for investigating the boundary in nanotube flow. At this point, it can be concluded that the flow boundary varies between the D and D' position depending on the applied pressure drop ΔP, but it is mostly close to D' which is the peak density or absorbed layer position.

Next, we use the slip length added MHP, Eq. (5), to observe the BP more closely, by varying the input energy, $\int PdV$, and thermodynamic states using temperature (T). As explained in the previous section, the energy distribution of our system was governed by the input energy or work done $\int PdV$. On the other hand, higher temperature will increase the kinetic movement of molecules, and consequently, the probability of momentum exchange will be higher. Thus, we also implemented $T = 120$ K and $T = 100$, K in our simple liquid system confined in the CNT, and kept ρ_{bulk} at 0.8. In brief, we changed the thermodynamic state for this analysis to observe how that affected the BP Figures 8(a) and 8(b) present the $T = 100$ K system with $\Delta P = 39.3$ MPa and $\Delta P = 55.2$ MPa, respectively, and Figs. 8(c) and 8(d) show the $T = 120$ K system with $\Delta P = 37.2$ MPa and $\Delta P = 52.2$ MPa, respectively. It is important to include that the experimental viscosity for $T = 120$ K argon was collected from Ref. [26] and was $1.77 \pm 0.17 \times 10^{-4}$ Pa s. The BP surprised us by varying its locality. We can see that the BP for all four cases in Figs. 8(a)–8(d) varies from the solid wall position of D to the peak density position D', as far as 1.4σ away from the innermost solid wall as the thermodynamic properties in our analysis vary, with most cases being closer to the peak density point D' than the solid wall position D. Such boundary shift can also be observed in the prediction of the volumetric flow rate. The NEMD data for the volumetric flow rate are calculated using the concentration gradient, $\partial N/\partial t V_{\text{Ar}}$, where N is the number of argon molecules and V_{Ar} is the molecular volume of argon. We also utilized the no-slip HP assumption and the slip length added MHP, Eqs. (2) and (4), respectively, to observe the BP more meticulously. This analysis was based

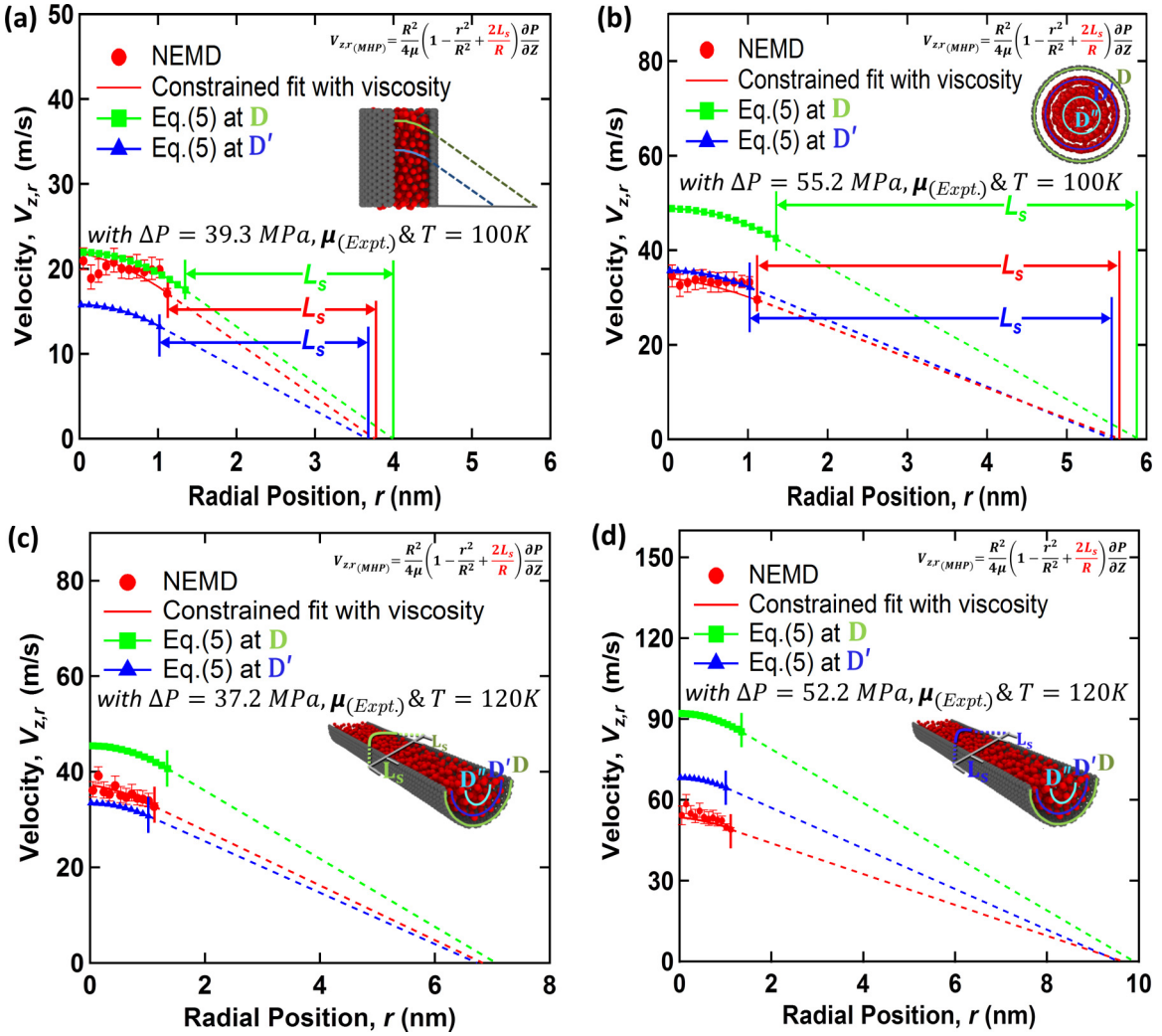

FIG. 8. Effect of temperature on the comparison of the velocity profiles from the NEMD simulations and the slip length added modified Hagen-Poiseuille (MHP) equation: (a), (b) 100 K system temperature with $\Delta P = 39.3$ and 55.2 MPa, respectively; (c), (d) 120 K system temperature with $\Delta P = 37.2$ and 52.2 MPa, respectively.

on volumetric flow rate, varying the input energy, $\int PdV$, and thermodynamic states using different temperatures (T), Figs. 9(a)–9(d). Figures 9(a) and 9(b) show the fundamental HP assumptions for the volumetric flow rate are for the 100 and 120 K systems, respectively. Figures 9(c) and 9(d) extend the MHP by the slip length to make the flow rate prediction, including the effect of varying input energy and temperatures. BP still varies from the solid wall position of D to the peak density position D', while increasing the temperature. The breakdown of the no-slip HP assumptions by several orders at the nanoscale is demonstrated again in Figs. 9(a) and 9(b) from the perspective of the volumetric flow rate. A boundary shift is also evident in Figs. 9(c) and 9(d) as in previous discussions. The velocity profile and volumetric flow rate are expected to be closely correlated.

Therefore, the BP varies during the nanoscale flow of a simple liquid through a CNT, but why? The boundary shift begins to increase with higher pressure drops. Even an incremental change in system temperature (T) increases the shift, so BP $= f\{\Delta P,\ T\}$. It can be understood that the overall velocity profile increases as more work, $\int PdV$, is done on the system, but the flow boundary position is shifting too. The first law of thermodynamics, the law of conservation of energy [Eq. (14)], indicates some divergence of energy from kinetic energy formalism upon the incremental changes in the energy input into the system. The effects of van der Waals or intermolecular forces during nanoconfinement explain that occurrence. Therefore, the effects of the potential energy operator and the kinetic energy operator in the Hamiltonian ($\hat{H}$) of our system might resolve this issue. For simplicity, we assume that a potential energy barrier ($E_{P,\text{barrier}}$) is the reason for the divergence, That barrier increases as the ΔPs and T increase: $E_{P,\text{barrier}}$ is an obstruction to the transformation of input energy into the expected kinetic energy (E_K). The simple liquid molecules have to overcome $E_{P,\text{barrier}}$ during their movement through CNT. Thus, a higher $E_{P,\text{barrier}}$ consumes a larger portion of the energy input to enable flow through the CNT. The notion of a potential energy barrier is acquired from the work of Babu and Sathian [83], which was based on incorporating Eyring theory

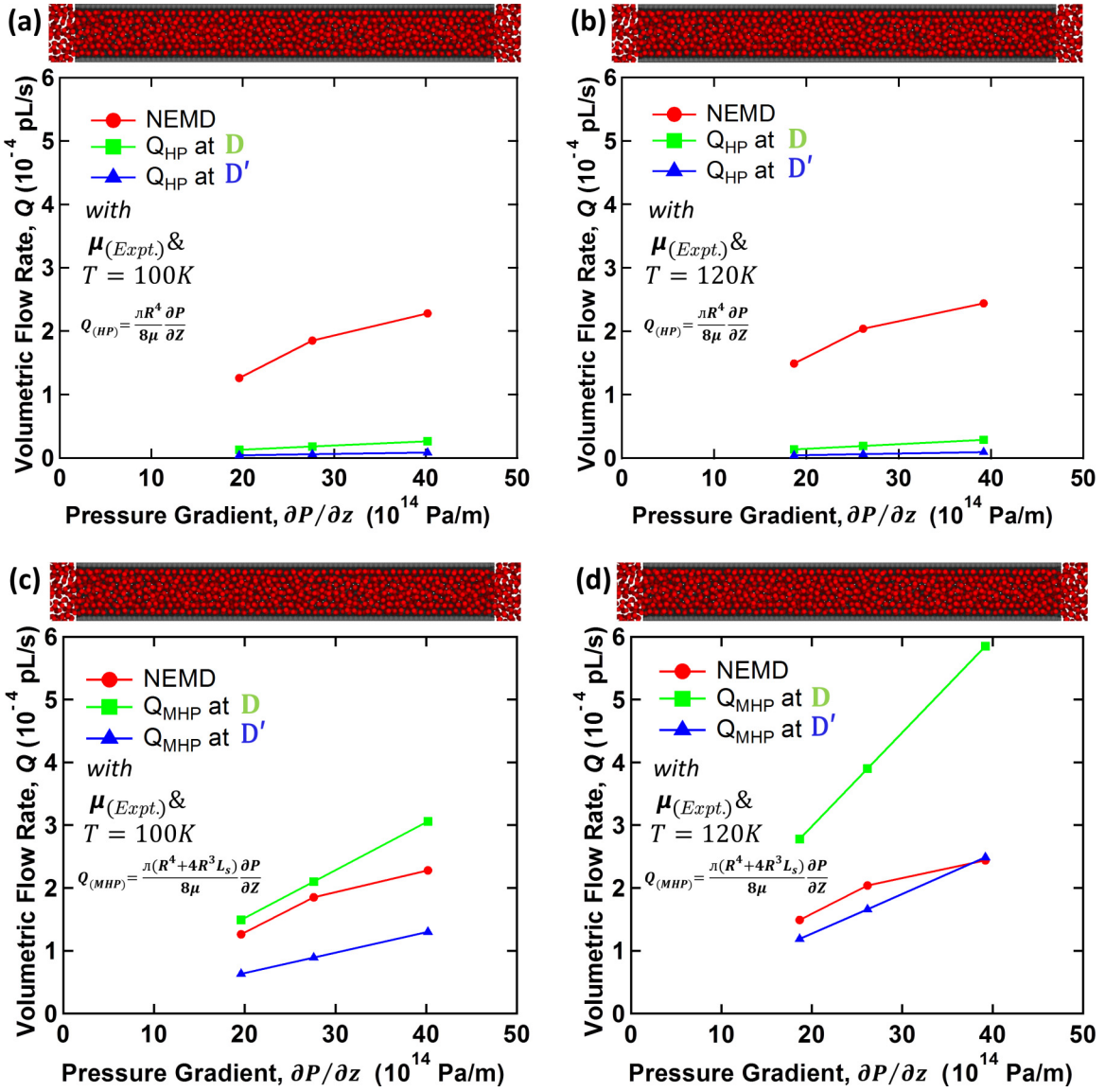

FIG. 9. A comparison of the volumetric flow rate with respect to pressure gradient from the NEMD simulations and Hagen-Poiseuille (HP) assumptions with different system temperatures: (a), (b) Fundamental HP assumptions at different boundary positions for 100 and 120 K system temperatures, respectively; (c), (d) Modified HP (MHP) assumptions at different boundary positions for 100 and 120 K system temperatures, respectively.

into molecular flow. In that context, $E_{P,\text{barrier}}$ is defined as $|E_{P,\text{equilibrium}} - E_{P,\text{nonequilibrium},\Delta P}|$. Analyzing the liquid argon data in the CNT from the equilibrium and nonequilibrium states shows that when ΔP increases along with the temperature (T), the ratio ($E_{P,\text{barrier}}/E_K$) increases. The value of $E_{P,\text{barrier}}/E_K$ has been acquired as 0.39, 0.78, 2.94, and 5.8 when the boundary shift (Δ) is 0.32σ, 0.54σ, 0.68σ, and 1.4σ, respectively: $\Delta \propto \frac{E_{P,barrier}}{E_K}$. On the other hand, the shear stress or the friction force between the liquid argon and carbon molecules also increases with the input energy, which limits the ability of the liquid argon molecules to overcome the increased energy barrier. In short, the ratio of potential energy barrier to kinetic energy is one possible explanation for the shift of the boundary position away from the innermost solid wall.

V. CONCLUSION

In summary, we have here used NEMD simulations of a simple liquid flow through a SWCNT to examine the ambiguity in defining nanoscale boundaries. Our EMD simulations support our NEMD interpretations, which were based on the first law of thermodynamics. Varying the maximum radius of the cylindrical bin alters the density distribution prediction by including and excluding the interfacial empty region or depletion length, which also signifies the multiple phases in the CNT. Therefore, the probability function for number density, $p(\rho_{\text{liquid},\text{CNT}})$, effectively describes the nanoscale effects of flow in a CNT. We next consider the deduction of a no-slip case at the nanoscale. Adjusting the interaction parameters produced convergence between the NEMD results and the no-slip HP assumptions at the nanoscale. Those calculations

indicate that the boundary position lies between the innermost solid wall (D) and the peak density or absorbed layer position (D'). We also presented the effects of viscosity, pressure, and temperature on the flow boundary in a SWCNT. The boundary positions depend on the input energy or work done on the system and the thermodynamic state of the system. The first law of thermodynamics indicates a considerable divergence of energy with the incremental changes to the energy input into the system, which creates a barrier to the transformation of that input energy into the expected kinetic energy, which causes the flow boundary position to vary. The effects of intermolecular forces and the nanoconfinement cause those events. In the end, we conclude that the ratio of the potential energy barrier to kinetic energy is proportional to the shift in the boundary position from the innermost solid wall at the nanoscale.

ACKNOWLEDGMENTS

This work was supported by the National Research Foundation of Korea (NRF) grant funded by the Korea government (MSIT) (Grant No. NRF-2019R1A2C1004661).

[1] C. Dekker, Carbon nanotubes as molecular quantum wires, Phys. Today **52**(5), 22 (1999).
[2] S. Iijima and T. Ichihashi, Helical microtubules of graphitic carbon, Nature **354**, 56 (1991).
[3] L. Langer, V. Bayot, E. Grivei, J.-P. Issi, J. P. Heremans, C. H. Olk, L. Stockman, C. Van Haesendonck, and Y. Bruynseraede, Quantum Transport in a Multiwalled Carbon Nanotube, Phys. Rev. Lett. **76**, 479 (1996).
[4] L. V. Mirantsev, Superfluidity inside carbon nanotubes, Phys. Rev. E **100**, 023106 (2019).
[5] S. Joseph and N. R. Aluru, Why are carbon nanotubes fast transport of water?, Nano Lett. **8**, 452 (2008).
[6] C. Wang, M. Waje, X. Wang, J. M. Tang, R. C. Haddon, and Y. Yan, Proton exchange membrane fuel cells with carbon nanotube based electrodes, Nano Lett. **4**, 345 (2004).
[7] B. Corry, Designing carbon nanotube membranes for efficient water desalination, J. Phys. Chem. B **112**, 1427 (2008).
[8] J. Wang, Carbon-nanotube based electrochemical biosensors: A review, Electroanalysis **17**, 7 (2005).
[9] M. M. Shulaker, G. Hills, N. Patil, H. Wei, H.-Y. Chen, H.-S. P. Wong, and S. Mitra, Carbon nanotube computer Nature **501**, 526 (2013).
[10] J. K. Holt, H. G. Park, Y. Wang, M. Stadermann, A. B. Artyukhin, C. P. Grigoropoulos, A. Noy, and O. Bakajin, Fast mass transport through sub-2-nanometer carbon nanotubes, Science **312**, 1034 (2006).
[11] M. Majumder, N. Chopra, R. Andrews, and B. J. Hinds, Enhanced flow in carbon nanotubes, Nature **438**, 44 (2005).
[12] G. Hummer, J. C. Rasaiah, and J. P. Noworyta, Water conduction through the hydrophobic channel of a carbon nanotube, Nature **414**, 188 (2001).
[13] A. I. Skoulidas, D. M. Ackerman, J. K. Johnson, and D. S. Sholl, Rapid Transport of Gases in Carbon Nanotubes, Phys. Rev. Lett. **89**, 185901 (2002).
[14] E. Secchi, S. Marbach, A. Nigues, D. Stein, A. Siria, and L. Bocquet, Massive radius-dependent flow slippage in carbon nanotubes, Nature **537**, 210 (2016).
[15] K. Falk, F. Sedlmeier, L. Joly, R. R. Netz, and L. Bocquet, Molecular origin of fast water transport in carbon nanotube membranes: Superlubricity versus curvature dependent friction, Nano Lett. **10**, 4067 (2010).
[16] P. L. Kapitza, Heat transfer and superfluidity of helium II, Phys. Rev. **60**, 354 (1941).
[17] B. H. Kim, A. Beskok, and T. Cagin, Thermal interactions in nanoscale fluid flow: Molecular dynamics simulations with solid–liquid interfaces, Microfluid. Nanofluid. **5**, 551 (2008).
[18] T. Q. Vo and B. Kim, Interface thermal resistance between liquid water and various metallic surfaces, Int. J. Precis. Eng. Manuf. **16**, 1341 (2015).
[19] H. Zhong and J. R. Lukes, Interfacial thermal resistance between carbon nanotubes: Molecular dynamics simulations and analytical thermal modeling, Phys. Rev. B **74**, 125403 (2006).
[20] L. Monniello, H. N. Tran, R. Vialla, G. Prevot, S. Tahir, T. Michel, and V. Jourdain, Comprehensive model of the optical spectra of carbon nanotubes on a substrate by polarized microscopy, Phys. Rev. B **99**, 115431 (2019).
[21] M. E. Weese, R. A. Krevh, Y. Li, N. T. Alvarez, and A. E. Ross, Defect sites modulate fouling resistance on carbon-nanotube fiber electrodes, ACS Sens. **4**, 1001 (2019).
[22] D. N. Futaba, K. Hata, T. Yamada, K. Mizuno, M. Yumura, and S. Iijima, Kinetics of Water-Assisted Single-Walled Carbon Nanotube Synthesis Revealed by a Time-Evolution Analysis, Phys. Rev. Lett. **95**, 056104 (2005).
[23] J. Prasek, J. Drbohlavova, J. Chomoucka, O. Jasek, J.Hubalek, V. Adam, and R. Kizek, Methods for carbon nanotubes systhesis, J. Mater. Chem. **21**, 15872 (2011).
[24] S. P. Sutera and R. Skalak, The history of Poiseuille's law, Annu. Rev. Fluid Mech. **25**, 1 (1993).
[25] J. Pfitzner, Poiseuille and his law, Anaesthesia **31**, 273 (1976).
[26] S. K. Kannam, B. D. Todd, J. S. Hansen, and P. J. Daivis, Slip flow in graphene nanochannels, J. Chem. Phys. **135**, 016313 (2011).
[27] Z. Liang and P. Keblinski, Slip length crossover on a graphene surface, J. Chem. Phys. **142**, 134701 (2015).
[28] H. Yasuoka, R. Takahama, M. Kaneda, and K. Suga, Confinement effects on liquid-flow characteristics in carbon nanotubes, Phys. Rev. E **92**, 063001 (2015).
[29] A. Barati Farimani and N. R. Aluru, Existence of multiple phases of water at nanotube interfaces, J. Phys. Chem. C **120**, 23763 (2016).
[30] J. H. Walther, K. Ritos, E. R. Cruz-Chu, C. M. Megaridis, and P. Koumoutsakos, Barriers to superfast water transport in carbon nanotube membranes, Nano Lett. **13**, 1910 (2013).
[31] J. A. Thomas and A. J. H. McGaughey, Reassessing fast water transport through carbon nanotubes, Nano Lett. **8**, 2788 (2008).
[32] M. E. Suk and N. R. Aluru, Modeling water flow through carbon nanotube membranes with entrance/exit effects, Nanoscale Microscale Thermophys. Eng. **21**, 247 (2017).

[33] S. K. Kannam, B. D. Todd, J. S. Hansen, and P. J. Daivis, Slip length of water on graphene: Limitations of non-equilibrium molecular dynamics simulations, J. Chem. Phys. **136**, 024705 (2012).

[34] J. Li, D. Liao, and S. Yip, Coupling continuum to molecular-dynamics simulation: Reflecting particle method and the field estimator, Phys. Rev. E **57**, 7259 (1998).

[35] F. Zhu, E. Tajkhorshid, and K. Schulten, Theory and simulation of water permeation in aquaporin-1, Biophys. J. **86**, 50 (2004).

[36] G. J. Wang and N. G. Hadjiconstantinou, Why are fluid densities so low in carbon nanotubes? Phys. Fluids **27**, 052006 (2015).

[37] I. Hanasaki and A. Nakatani, Flow structure of water in carbon nanotubes: Poiseuille type or plug-like? J. Chem. Phys. **124**, 144708 (2006).

[38] I. Bitsanis, J. J. Magda, M. Tirrell, and H. T. Davis, Molecular dynamics of flow in micropores, J. Chem. Phys. **87**, 1733 (1987).

[39] T. Q. Vo, M. Barisik, and B. Kim, Atomic density effects on temperature characteristics and thermal transport at grain boundaries through a proper bin size selection, J. Chem. Phys. **144**, 194707 (2016).

[40] M. R. Hasan and B. H. Kim, Molecular transport phenomena of simple liquids through a nanoporous graphene membrane, Phys. Rev. E **102**, 033110 (2020).

[41] X. Chen, G. Cao, A. Han, V. K. Punyamurtula, L. Liu, P. J. Culligan, T. Kim, and Y. Qiao, Nanoscale fluid transport: Size and rate effects, Nano Lett. **8**, 2988 (2008).

[42] A. Sam, V. Prasad, and S. P. Sathian, Water flow in carbon nanotubes: The role of tube chirality, Phys. Chem. Chem. Phys. **21**, 6566 (2019).

[43] B. H. Kim, A. Beskok, and T. Cagin, Viscous heating in nanoscale shear driven liquid flows, Microfluid. Nanofluid. **9**, 31 (2010).

[44] T. Q. Vo, M. Barisik, and B. H. Kim, Near-surface viscosity effects on capillary rise of water in nanotubes, Phys. Rev. E **92**, 053009 (2015).

[45] C. Bakli and S. Chakraborty, Anomalous interplay of slip, shear and wettability in nanoconfined water, Nanoscale **11**, 11254 (2019).

[46] P. A. Thompson and S. M. Troian, A general boundary condition for liquid flow at solid surface, Nature **389**, 360 (1997).

[47] M. Barisik and A. Beskok, Equilibrium molecular dynamics studies on nanoscale-confined fluids, Microfluid. Nanofluid. **11**, 360 (2011).

[48] L. Bocquet and J. L. Barrat, Hydrodynamic boundary conditions, correlation functions, and Kubo relations for confined fluids, Phys. Rev. E **49**, 3079 (1994).

[49] L. Bocquet and J. L. Barrat, On the Green-Kubo relationship for the liquid-solid friction coefficient, J. Chem. Phys. **139**, 044704 (2013).

[50] K. Huang and I. Szlufarska, Green-Kubo relation for friction at liquid-solid interface, Phys. Rev. E **89**, 032119 (2014).

[51] B. Ramos-Alvarado, S. Kumar, and G. P. Peterson, Hydrodynamic slip length as a surface property, Phys. Rev. E **93**, 023101 (2016).

[52] H. Oga, Y. Yamaguchi, T. Omori, S. Merabia, and L. Joly, Green-Kubo measurement of liquid-solid friction in finite-size systems, J. Chem. Phys. **152**, 054502 (2019).

[53] O. Vincent, A. Szenicer, and A. D. Stroock, Capillarity-driven flows at the continuum limit, Soft Matter **12**, 6656 (2016).

[54] S. Gruener, T. Hofmann, D. Wallacher, A. V. Kityk, and P. Huber, Capillary rise of water in hydrophilic nanopores, Phys. Rev. E **79**, 067301 (2009).

[55] S. Gruener and P. Huber, Spontaneous Imbibition Dynamics of an *n*-Alkane in Nanopores: Evidence of Meniscus Freezing and Monolayer Sticking, Phys. Rev. Lett. **103**, 174501 (2009).

[56] A. T. Pham, M. Barisik, and B. Kim, Molecular dynamics simulations of Kapitza length for argon-silicon and water-silicon interfaces, Int. J. Precis. Eng. Manuf. **15**, 323 (2014).

[57] M. Barisik and A. Beskok, Temperature dependence of thermal resistance at the water/silicon interface, Int. J. Therm. Sci. **77**, 47 (2014).

[58] B. Ramos-Alvarado, S. Kumar, and G. P. Peterson, Solid–liquid thermal transport and its relationship with wettability and the interfacial liquid structure, J. Phys. Chem. Lett. **7**, 3497 (2016).

[59] R. Bhadauria and N. R. Aluru, A quasi-continuum hydrodynamic model for slit shaped nanochannel flow, J. Chem. Phys. **139**, 074109 (2013).

[60] J. Koplik, J. R. Banavar, and J. F. Willemsen, Molecular dynamics of fluid flow at solid surfaces, Phys. Fluids A **1**, 781 (1989).

[61] J. Ghorbanian, A. T. Celebi, and A. Beskok, A phenomenological continuum model for force-driven nano-channel liquid flows, J. Chem. Phys. **145**, 184109 (2016).

[62] C. Herrero, T. Omori, Y. Yamaguchi, and L. Joly, Shear force measurement of the hydrodynamic wall position in molecular dynamics, J. Chem. Phys. **151**, 041103 (2019).

[63] M. Masuduzzaman and B. Kim, Scale effects in nanoscale heat transfer for Fourier's law in a dissimilar molecular interface, ACS Omega **5**, 26527 (2020).

[64] C.-L. Navier, Mémoire sur les lois du mouvement des fluides, Mem. Acad. Sci. Inst. Fr. **6**, 389 (1823).

[65] G. G. Stokes, On the effect of the internal friction of fluids on the motion of pendulums, Trans. Cambridge Philos. Soc. **9**, 8 (1851).

[66] G. E. Karniadakis, A. Beskok, and N. Aluru, *Microflows and Nanoflows: Fundamentals and Simulation* (Springer, New York, 2005).

[67] T. S. Ingebrigtsen, T. B. Schrøder, and J. C. Dyre, What Is a Simple Liquid? Phys. Rev. X. **2**, 011011 (2012).

[68] C. T. Nguyen and A. Beskok, Saltwater transport through pristine and positively charged graphene membranes, J. Chem. Phys. **149**, 024704 (2018).

[69] H. G. Ozcelik, A. C. Ozdemir, B. Kim, and M. Barisik, Wetting of single crystalline and amorphous silicon surfaces: Effective range of intermolecular forces for wetting, Mol. Simul. **46**, 224 (2020).

[70] M. P. Allen and D. J. Tildesley, *Computer Simulation of Liquids* 2nd ed. (Oxford University Press, Oxford, 2017).

[71] T. Q. Vo and B. Kim, Transport phenomena of water in molecular fluidic channels, Sci. Rep. **6**, 33881 (2016).

[72] A. Tenenbaum, Local equilibrium in stationary states by molecular dynamics, Phys. Rev. A **28**, 3132 (1983).

[73] B. Kim, A. Beskok, and T. Cagin, Molecular dynamics simulations of thermal resistance at the liquid-solid interface, J. Chem. Phys. **129**, 174701 (2008).

[74] A. Pham, M. Barisik, and B. Kim, Pressure dependence of Kapitza resistance at gold/water and silicon/water interfaces, J. Chem. Phys. **139**, 244702 (2013).

[75] K. Cho and J. D. Joannopoulos, Ergodicity and dynamical properties of constant-temperature molecular dynamics, Phys. Rev. A **45**, 7089 (1992).

[76] Q. Kim and W. Jhe, Interfacial thermodynamics of spherical nanodroplets: Molecular understanding of surface tension via a hydrogen bond network, Nanoscale **12**, 18701 (2020).

[77] S. Plimpton, Fast parallel algorithms for short-range molecular dynamics, J. Comput. Phys. **117**, 1 (1995).

[78] J. H. Irving and J. G. Kirkwood, The statistical mechanical theory of transport processes. IV. The equations of hydrodynamics, J. Chem. Phys. **18**, 817 (1950).

[79] B. D. Todd, D. J. Evans, and P. J. Daivis, Pressure tensor for inhomogeneous fluids, Phys. Rev. E **52**, 1627 (1995).

[80] B. Hess, Determining the shear viscosity of model liquids from molecular dynamics simulations, J. Chem. Phys. **116**, 209 (2002).

[81] L. Cheng, P. Fenter, K. L. Nagy, M. L. Schlegel, and N. C. Sturchio, Molecular-Scale Density Oscillations in Water Adjacent to a Mica Surface, Phys. Rev. Lett. **87**, 156103 (2001).

[82] F. Heslot, N. Fraysse, and A. M. Cazabat, Molecular layering in the spreading of wetting liquid drops, Nature **338**, 6656 (1989).

[83] J. S. Babu and S. P. Sathian, The role of activation energy and reduced viscosity on the enhancement of water flow through carbon nanotubes, J. Chem. Phys. **134**, 194509 (2011).